Sensors and Materials, Vol. 38, No. 4 (2026) 1941–1957
MYU Tokyo

S & M 4417

Optimal Configuration of Energy Storage Considering Photovoltaic Integration in Distribution Networks

Lingling Li,[1,2] Haowen Xu,[1,2] Hsiung-Cheng Lin,[3*] and Zishuo Xu[4]

[1]State Key Laboratory of Intelligent Power Distribution Equipment and System, Hebei University of Technology, Tianjin 300401, China
[2]Key Laboratory of Electromagnetic Field and Electrical Apparatus Reliability of Hebei Province, Hebei University of Technology, Tianjin 300401, China
[3]Department of Electronic Engineering, National Chin-Yi University of Technology. Taichung 41170, Taiwan
[4]College of Software, Jilin University, Changchun 132200, China

(Received November 25, 2025; accepted February 17, 2026)

Keywords: energy storage, photovoltaic sensor, photovoltaic integration, mirage search optimization

In the context of high-penetration renewable energy integration, the increasing adoption of photovoltaic (PV) systems gives rise to significant operational challenges to power grids owing to the inherent intermittency and volatility of solar energy resources. Energy storage (ES) systems, with their flexible regulation capabilities, have been widely deployed to mitigate the impact of renewable generation fluctuations. However, existing methodologies often fail to adequately balance PV integration levels with system economic viability, which hinders the large-scale deployment of ES. To address this issue, we establish a PV integration cost metric to coordinate the integration effectiveness and economic benefits. The ES systems can therefore be leveraged by enhancing the PV hosting capacity in distribution networks. PV sensors are also employed to collect irradiance data, which, combined with load profiles, enable optimized power supply–demand matching through demand response strategies. Furthermore, the mirage search optimization algorithm is applied to improve computational efficiency, ultimately deriving the optimal ES configuration. The superiority of the algorithm is verified through a comparative analysis of the convergence performance on benchmark test functions. Simulation results demonstrate that the proposed model effectively increases the PV integration rate while reducing operational costs by approximately 8.19%, confirming its dual advantages in both economic efficiency and technical benefits.

1. Introduction

As the global energy crisis and climate change issues have become increasingly severe around the world, there is a worldwide consensus on transitioning the energy structure towards cleaner and low-carbon sources.(1) As a key pathway to achieving the "carbon peak and carbon neutrality" goals, renewable energy, particularly photovoltaic (PV) power, has experienced explosive growth in recent years.(2,3) Among these, distributed PVs have seen large-scale

*Corresponding author: e-mail: hclin@ncut.edu.tw
https://doi.org/10.18494/SAM6079

ISSN 0914-4935
https://myukk.org/

deployment at the distribution network level owing to advantages such as flexible siting, the local consumption of electricity, and short construction cycles. With its penetration rate continuing to rise, PV is profoundly reshaping the structure and operation of traditional distribution networks.[4,5]

However, PV power generation exhibits significant intermittency, randomness, and volatility, thus posing unprecedented challenges to distribution networks.[6] When PV penetration reaches its high levels, its reverse power flow can easily cause line voltage violations. During periods of abundant solar irradiation and low load, the distribution network's PV hosting capacity may reach its limit, forcing the system to adopt "PV curtailment" measures. This not only leads to a waste of clean energy but also hinders the sustainable development of the PV industry. Through the coordinated operation of energy storage (ES) and PV systems, it is possible to effectively mitigate power fluctuations, shave peaks and fill valleys, and regulate voltage, thereby maximizing the utilization of solar power while ensuring the safety and stability of the grid.[7] Therefore, in-depth research on the coordinated planning and operation strategies of PV and ES in distribution networks is of great significance for enhancing PV integration and supporting the development of new-type power systems.[8–10]

The rapid advancement of sensor technology has injected new momentum into the coordinated planning of PVs and ES.[11] In recent years, PV sensors have achieved significant improvements in key performance metrics, particularly in measurement accuracy, detection range, and environmental adaptability. Integrated environmental sensors capable of monitoring multiple meteorological parameters, such as TH-WQX7, are able to provide more accurate data support for PV power forecasting.[12] These technological developments enable power systems to collect multidimensional, high-resolution operational data, laying a solid foundation for optimizing energy management strategies.

To address the challenges posed by high PV penetration rate, extensive studies in PV integration assessment, ES deployment, and PV-storage coordination have been conducted worldwide. Regarding ES system applications, existing research primarily has been focused on how site selection and capacity determination impact system economics. For instance, in some studies, storage configurations were optimized by mitigating PV fluctuations, enabling peak–valley arbitrage, reducing network losses, and lowering carbon emission costs.[13,14] Wang *et al.*[15] examined the impact of user load management on system capacity allocation and associated economic viability, but they targetted solely distribution network operating costs and thus failed to comprehensively address actual operational requirements, potentially leading to significant discrepancies between the findings and real-world conditions. Although existing research has laid a solid foundation, most studies emphasize a single objective such as economic efficiency or stability, lacking a coordinated optimization framework that comprehensively considers integration rates and system costs. For instance, Nengroo *et al.*[16] employed an energy management strategy to enhance the system's economic performance, but it lacked a coordination mechanism between the investment costs of PV and ES systems. Wang *et al.*[17] improved the system's PV integration capacity by employing electric vehicle (EV) dispatch and ES system configuration strategies. They analyzed the effectiveness of this approach under

different scenarios, but economic efficiency and integration capacity were not coordinated, implying no trade-off between these two issues.

In this study, we develop an ES configuration model to enhance the grid integration capability of PV systems in distribution networks. The remaining sections are as follows. In Sect. 2, we present the optimization allocation model for ES. In Sect. 3, the improved strategy for the improved mirage search optimization (IMSO) is described and its effectiveness is verified through the comparative testing of objective functions. Section 4 includes the validation of the effectiveness of the optimization allocation model in enhancing the system's PV integration capacity through case-based analysis. In Sect. 5, we summarize our conclusions and future outlook.

2. System Model

2.1 PV model

In PV systems, PV sensors accurately measure solar irradiance to obtain light intensity data. In this study, we employ the Apogee SP-series SP-110 self-powered shortwave radiation sensor. This sensor comprises a photodiode, signal-processing circuitry, and cable, all housed in an aluminum oxide enclosure. It features a fully solid-state encapsulation without internal air gaps, a design specifically intended for the continuous measurement of total shortwave radiation under outdoor conditions. The analog output from the SP series sensor is directly proportional to the intensity of the incident total shortwave radiation. In this study, the sensor was mounted using a specialized bracket to maintain a strictly horizontal and skyward orientation. The installation site was selected to ensure a complete lack of obstructions throughout the year, thereby securing the accuracy and representativeness of the acquired data.

Given that PV output exhibits significant intermittency and stochasticity, its daily variation can be effectively characterized by the Beta distribution probability model. Therefore, using the real-time light intensity data acquired by the sensors, we can simulate the time-varying power output of the PV array throughout the day, generating what is known as the PV output curve. The specific formula for fitting the PV output is

$$f(i) = \frac{\Gamma(\alpha+\beta)}{\Gamma(\alpha)\Gamma(\beta)} i^{(\alpha-1)}(1-i)^{(\beta-1)}. \tag{1}$$

Here, i represents the irradiance of sunlight and α and β are shape parameters.

2.2 ES site preselection

The core objective of this study is to enhance the distribution network's capacity to accommodate distributed PV resources. To maximize the PV hosting capacity at each node after integrating ES systems, we propose to install ES at the nodes with the weakest PV integration utility. A PV integration utility index is developed to quantitatively evaluate the hosting capacity

of individual nodes. Nodes are ranked on the basis of this index, with the lowest 25% selected as candidate locations for ES installation. The specific calculation formula is

$$C_{ON,n} = \sum_{t=6}^{17} \frac{P_{pv,t} - 33 \cdot P_{l,t,n}}{P_{pv,t}}. \tag{2}$$

Here, $C_{ON,n}$ represents the PV absorption capacity of each node; $P_{pv,t}$ represents the PV power generation at time t; and $P_{l,t,n}$ indicates the load power at each node at time t.

2.3 Objective function

2.3.1 PV integration cost

The high cost of ES remains one of the central challenges hindering the widespread adoption of PV. To address this, we construct a PV cost-utility ratio function that balances economic viability with grid integration requirements, rather than merely treating it as a penalty for insufficient PV absorption. This function quantifies the cost incurred by the system to achieve a unit of absorption utility as

$$\begin{cases} C_{pi} = \sum_{t}^{24} \dfrac{\lambda \cdot C_{sys}}{1 - \exp\left(-k \cdot \dfrac{P_{pvu,t}}{P_{pvt,t}} \right)}, & i \neq 0 \\ C_{pi} = 0, & i = 0 \end{cases} \tag{3}$$

Here, λ represents the weighting coefficient for the system's economic costs and indicates the degree of emphasis placed on economic efficiency. k represents the absorption saturation coefficient, which indicates the degree of emphasis placed on the system's absorption capacity.

In this study, λ was set to 0.01 and k was set to 1. C_{sys} represents the total cost incurred by the system and is specifically expressed as $C_{sys} = C_{inv} + C_{op} + C_{pur} + C_{loss} + C_{dr}$. More details are as follows.

2.3.2 ES investment cost

Consider the capital investment required to configure ES for the system over its operational cycle. The ES investment cost C_{inv} represents a key factor in evaluating the economic viability of ES and is typically incorporated into the overall objective function as an equivalent cost.

$$C_{inv} = \frac{1}{365} \cdot \frac{\psi(1+\psi)^n}{(1+\psi)^n - 1} c_{inv,ES} E_{ES} \tag{4}$$

Here, ψ represents the discount factor, $c_{inv,ES}$ represents the investment cost per unit of ES, and n represents the planned operating years of the ES.

2.3.3 ES operating cost

To measure the operating costs incurred by ES systems during operation, the following formula is established to describe the operating cost per unit of energy exchanged.

$$C_{op} = \sum_{i=1}^{24} c_{inv,trans} P_{i,trans} \tag{5}$$

Here, $c_{inv,trans}$ represents the cost per unit power exchanged during ES charging and discharging.

2.3.4 Electricity purchase cost

Here, the cost incurred by the system for purchasing electricity from the upstream grid is calculated. It represents one of the primary cost components within the power system and is directly affected by electricity prices and policy measures.

$$C_{pur} = \sum_{t=1}^{24} c_t^{pur} P_t^{pur} \tag{6}$$

Here, c_t^{pur} represents the cost per unit of electricity purchased by the system.

2.3.5 Network loss cost

Next, we quantify the cost of losses incurred during the transmission of electrical energy within distribution networks. By calculating network losses, the algorithm is incentivized to seek more economical power flow distributions, thereby enhancing the overall economic efficiency of the system.

$$C_{loss} = \sum_{t=1}^{24} c_t^{loss} P_t^{loss} \tag{7}$$

Here, c_t^{loss} represents the network loss cost per unit of electricity of the system.

2.3.6 Demand response cost

The compensation fee paid to incentivize users to adjust their electricity load patterns, which represents the economic cost incurred to enhance system flexibility, is

$$C_{dr} = \sum_{t=1}^{24} c_{dr,load} P_t^{dr}. \tag{8}$$

Here, $c_{dr,load}$ represents the policy subsidy cost per unit of load participating in the demand response (DR) strategy within the system.

2.4 Model constraints

2.4.1 Charge constraint

The charge constraints of ES units define the permissible range of electrical charge variation, ensuring that the operational state of the ES system remains within the boundaries of its rated capacity and safety parameters.

$$ESC(t) = \begin{cases} ESC(t-1) + \dfrac{P_{i,trans} \cdot \Delta t}{E_{ES}} \\ ESC(t-1) - \dfrac{P_{i,trans} \cdot \Delta t}{E_{ES}} \end{cases} \tag{9}$$

Here, $ESC(t)$ represents the energy stored at time t; $P_{i,trans}$ denotes the exchange power during charging and discharging; and E_{ES} is the rated capacity of the ES system.

Both excessively low and excessively high remaining charge levels in ES systems will directly impact the systems' lifespan. Therefore, it is necessary to limit the magnitude of the remaining charge.

$$ESC_{min} \le ESC(t) \le ESC_{max} \tag{10}$$

Here, ESC_{max} and ESC_{min} represent the maximum and minimum remaining charges, respectively.

2.4.2 Node voltage constraint

Node voltage constraints are fundamental requirements for maintaining stable system operation. These constraints define the amplitude range for all node voltages, preventing them from exceeding specified limits.

$$U_{node,min} \le U_{node} \le U_{node,max} \tag{11}$$

Here, $U_{node,max}$ and $U_{node,min}$ represent the upper and lower limits of node voltage, respectively.

2.4.3 Power constraint

Power constraints define the balance between active power and reactive power for various units, ES, and loads within the system.

$$\begin{cases} P_i - U_i \sum_{j=1}^{N_n} U_j (G_{ij}\cos\theta_{ij} + B_{ij}\sin\theta_{ij}) = 0 \\ Q_i - U_i \sum_{j=1}^{N_n} U_j (G_{ij}\sin\theta_{ij} - B_{ij}\cos\theta_{ij}) = 0 \end{cases} \tag{12}$$

Here, P_i and Q_i represent the active power and reactive power of the system at node i; U_i and U_j represent the voltage at nodes i and j; and G_{ij} and B_{ij} represent the equivalent conductance and susceptance between nodes i and j, respectively. Moreover, θ_{ij} represents the impedance angle.

2.4.4 Branch transmission power constraint

Branch transmission power constraint is designed to limit the maximum transmission capacity of the line.

$$S_j \le S_{j,max} \tag{13}$$

Here, S_j represents the apparent power transmitted by line j and $S_{j,max}$ represents the maximum apparent power that line j is permitted to transmit.

3. Proposed IMSO Algorithm

The Mirage search optimization (MSO) algorithm is a metaheuristic optimization method proposed in 2025.[18] Its design draws inspiration from the natural optical phenomenon of mirages. Mirages typically occur under specific meteorological and geographical conditions. When the ground is heated by solar radiation, a temperature gradient forms, leading to an uneven distribution of atmospheric density and causing stratified changes in refractive index. Light bends as it refracts in the atmosphere, whereas the human brain assumes that light travels in straight lines. This discrepancy results in the observation of virtual images that do not actually exist. Mimicking this principle, MSO establishes two core strategies: the upper and lower mirage strategies, corresponding to global exploration and local exploitation, respectively, which work in synergy to solve complex optimization problems.

3.1 MSO algorithm

3.1.1 Superior mirage strategy

The distance between the current individual and the global optimal individual is given by

$$h_{ij} = \left| x_{best}^{t} - x_{ij} \right| \cdot rand + 1, \tag{14}$$

where x_{best}^{t} represents the global optimal solution and *rand* represents a random number between 0 and 1.

Angles α and β are generated as

$$\begin{cases} \alpha = rand \cdot \dfrac{\pi}{9}, \\ \beta = rand \cdot \left(\dfrac{\pi}{4} - \dfrac{\alpha}{2} \right). \end{cases} \tag{15}$$

Three scenarios are distinguished on the basis of the position of the incident ray relative to the horizontal reference normal and the relationship between the angle of incidence α and the angle of inclination β of the refractive index boundary layer. The physical essence simulates the position of the observation point as seen by the observer after total internal reflection occurs under different geometric conditions.

Case 1: The incident light is to the left of the horizontal reference normal.

$$\Delta x_{lo} = a \cdot \frac{\sin(\pi - 2\alpha - 2\beta) \cdot h_{ij} \cdot \sin\left(\dfrac{\pi}{2} + \beta \right)}{\sin(\alpha - \beta)\sin(\alpha - 2\beta)} \tag{16}$$

Case 2: The incident light is to the right of the normal, and $\beta < \alpha < \pi/2$.

$$\Delta x_{lo} = a \cdot \frac{\sin(\pi - 2\alpha + 2\beta) \cdot h_{ij} \cdot \sin\left(\dfrac{\pi}{2} - \beta \right)}{\sin(\pi - \alpha + \beta)\sin(\alpha - 2\beta)} \tag{17}$$

Case 3: The incident light is to the right of the normal, and $\beta < \alpha < \pi/2$.

$$\Delta x_{lo} = a \cdot \frac{\sin(-\pi + 2\alpha - 2\beta) \cdot h_{ij} \cdot \sin\left(\dfrac{\pi}{2} - \beta \right)}{\sin(\pi - \alpha + \beta)\sin(\pi - \alpha + 2\beta)} \tag{18}$$

The initial position update formula derived from the above equations is

$$x_{ij}^{t+1} = x_{ij}^{t} + \Delta x_{lo}. \tag{19}$$

3.1.2 Inferior mirage strategy

Distance h and direction D are calculated for two cases.
Case 1: Non-optimal individual

$$\begin{cases} h_{ij} = \left| x_{best}^{t} - x_{ij} \right| \cdot rand, \\ D = \dfrac{\left(x_{best}^{t} - x_{ij} \right) \cdot rand}{h_{ij}}. \end{cases} \tag{20}$$

Case 2: Optimal individual

$$\begin{cases} h_{ij} = \left| \pm 0.05 \cdot rand \right|, \\ D = \dfrac{\pm 0.05 \cdot rand}{h_{ij}}. \end{cases} \tag{21}$$

The angle γ between the refractive index stratification line and the stratification reference line ranges from 0 to π/2. The angle φ between the incident light and the normal at the observation point is constrained by two key conditions: the lower bound ensures that the refracted ray reaches the initial position at the minimum incident angle, while the upper bound ensures that the refracted ray hits the intersection of the refractive index stratification line and the horizontal reference line at the maximum incident angle. The angles γ and φ and the angle of refraction ω are given by the following initialization equations:

$$\begin{cases} \gamma = \dfrac{\pi(t_{max} - t)}{2t_{max}} \cdot rand, \\ \varphi = \left(\arctan\left(\dfrac{1}{2\tan\gamma} \right) - \arctan\left(\dfrac{\sin\gamma\cos\gamma}{1+\sin^2\gamma} \right) \right) \cdot rand + \arctan\left(\dfrac{\sin\gamma\cos\gamma}{1+\sin^2\gamma} \right), \\ \omega = \arcsin\left(\dfrac{n_2}{n_1} \sin(\varphi + \gamma) \right), \end{cases} \tag{22}$$

Here, t_{max} represents the maximum iteration count, t represents the current iteration count, n_1 is the refractive index below the refractive index stratification line, and n_2 is the refractive index above the refractive index stratification line.

The initial position update formulas derived from the above equations are

$$\Delta x_{up} = \frac{h}{\tan\gamma} - \frac{\left(\frac{h}{\sin\gamma} - \frac{h\sin\varphi}{\cos(\varphi+\gamma)}\right)\cos\omega}{\cos(\omega-\gamma)}, \tag{23}$$

$$x_{ij}^{t+1} = x_{ij}^{t} + D\Delta x_{up}. \tag{24}$$

3.2 Chaotic map

The MSO algorithm employs a random method to initialize the population, but it may suffer from low computational efficiency due to a poor distribution effect. In this study, we adopt a chaotic mapping initialization method to generate a strongly distributed discrete population with the following specific formula:

$$x_{i+1} = ax_i(1 - x_i), \tag{25}$$

Here, a is the control parameter, taking values within (0, 4). The larger the value of a, the higher the degree of chaos.

3.3 Reverse learning

To enhance the ability of the MSO algorithm to escape local optima, a reverse learning strategy is employed to obtain opposite solutions and broaden the exploration scope. The specific formula is

$$x_i^* = B_l + B_u - x_{best}^t, \tag{26}$$

Here, B_u and B_l represent the upper and lower bounds, respectively, and x_{best}^t denotes the optimal solution for t generation.

3.4 IMSO algorithm performance test

Two measures were carried out for the evaluation of the IMSO algorithm. Firstly, to comprehensively evaluate the optimization capabilities of the IMSO algorithm, performance comparison tests were conducted using six benchmark functions from CEC2005 and three representative algorithms. The test functions are presented in Table 1.

Secondly, the MSO, Mountaineering team-Based optimization (MBTO), Grey wolf optimizer (GWO), and IMSO algorithms on the selected CEC series test functions were used for

Table 1
Test functions used.

Function	Range
$F_1(x)=\sum_{i=1}^{n}x_i^2$	[−100, 100]
$F_2(x)=\sum_{i=1}^{n}\lvert x_i\rvert+\prod_{i=1}^{n}\lvert x_i\rvert$	[−10, 10]
$F_3(x)=\sum_{i=1}^{n}\left(\sum_{j=1}^{i}x_j\right)^2$	[−100, 100]
$F_4(x)=\sum_{i=1}^{11}\left[a_i-\frac{x_1\left(b_i^2+b_i x_2\right)}{b_i^2+b_i x_3+x_4}\right]^2$	[−100, 100]
$F_5(x)=\sum_{i=1}^{n-1}\left[100\left(x_{i+1}-x_i^2\right)^2+\left(x_i-1\right)^2\right]$	[−30, 30]
$F_6(x)=\sum_{i=1}^{n}([x_i+0.5])^2$	[−100, 100]

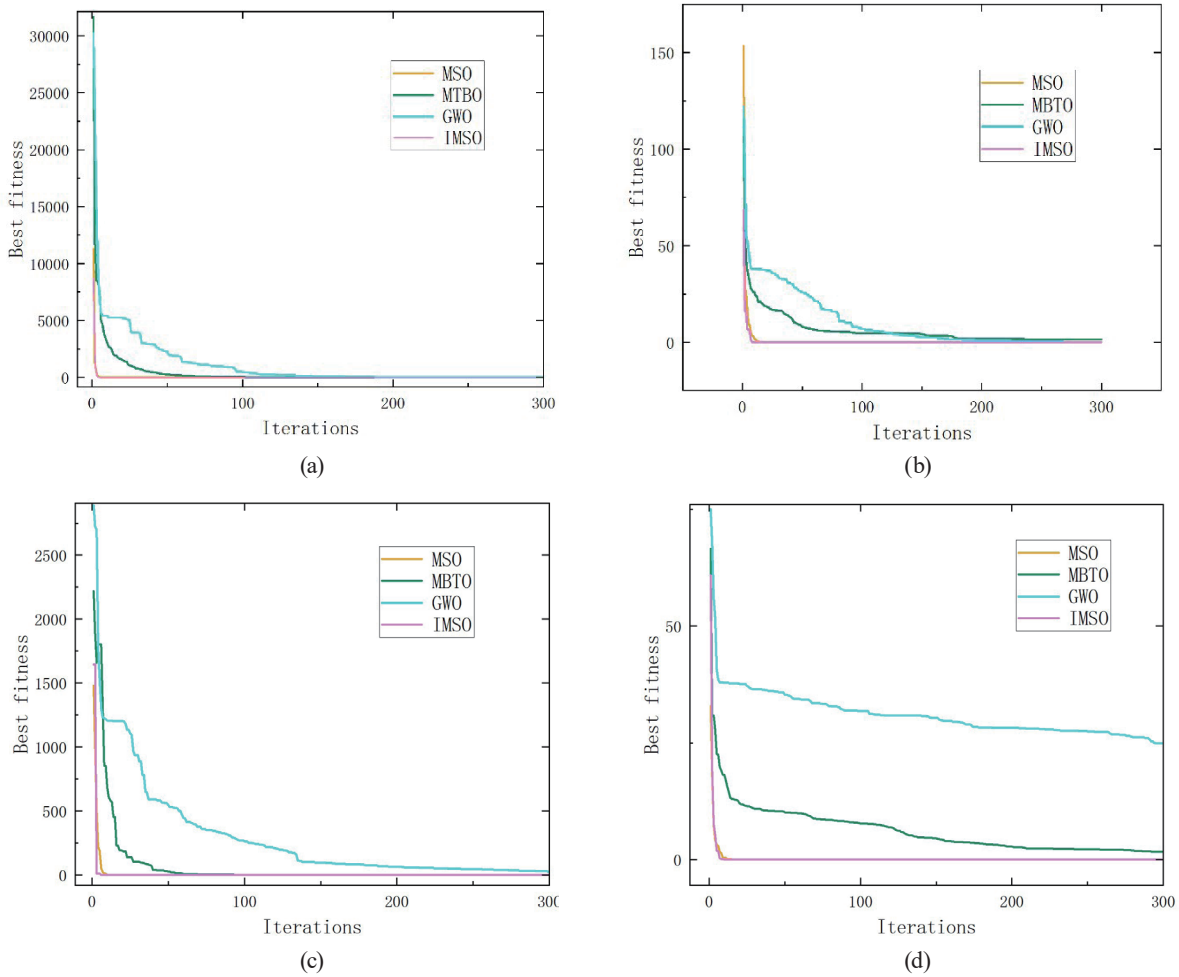

Fig. 1. (Color online) Curves of iterative results for each algorithm. (a) F1, (b) F2, (c) F3, (d) F4, (e) F5, and (f) F6.

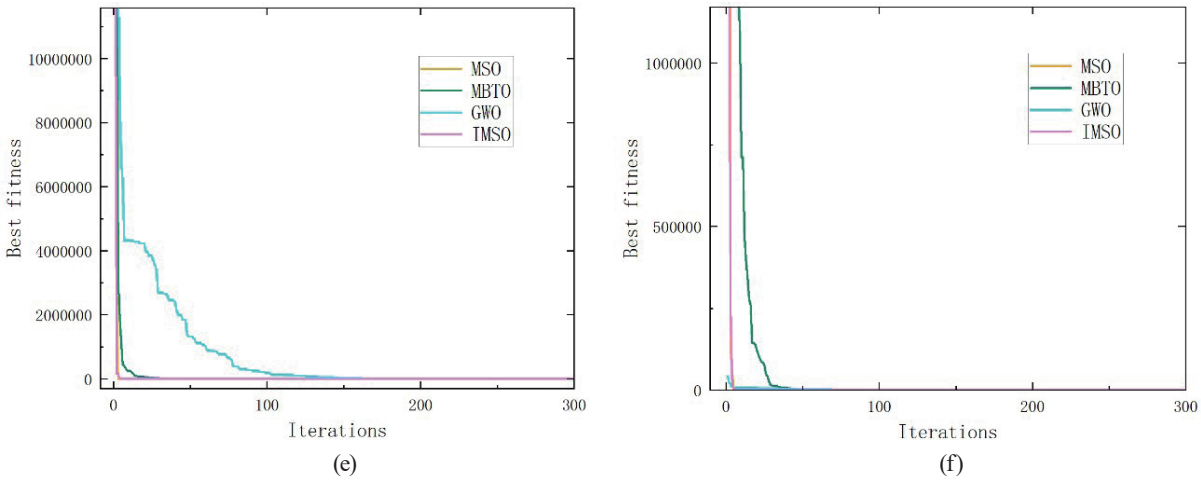

Fig. 1. (Continued) (Color online) Curves of iterative results for each algorithm. (a) F1, (b) F2, (c) F3, (d) F4, (e) F5, and (f) F6.

comparison in the iteration convergence response, as shown in Fig. 1. Performance results demonstrate that the IMSO algorithm exhibits superior convergence speed and accuracy in the initial stages compared with the selected comparison algorithms, proving the superior convergence performance of the IMSO algorithm.

4. Case Analysis

To validate the effectiveness of the proposed method, simulations were conducted for the IEEE 33-node test system. The distribution network topology is shown in Fig. 2, where ES can be deployed at nodes 1 to 33. The electricity price is shown in Table 2, and the parameters of ES and system specifications are shown in Table 3. The load data for each node, as shown in Fig. 3, cover the long-term typical operation period of the power system. The IMSO algorithm was employed to determine the location and capacity information for ES deployment. The validity of the proposed model was verified through comparative experiments under three scenarios. The PV output curve, fitted from the data sampled by PV sensors, is depicted in Fig. 4. The program flowchart is illustrated in Fig. 5. For the DR strategy, Fig. 6 illustrates the load before and after implementation.

To begin with, a pre-siting for ES was conducted. In pre-siting calculations, nodes with higher computed values absorb less PV power. From Fig. 7, eight nodes with the lowest PV absorption capacity are identified: 9, 11, 33, 6, 26, 16, 15, and 10. These nodes are then evaluated within the IEEE 33-node test system using an objective function focused on cost minimization. A lower ES planning cost reflects a higher economic efficiency for the system. Similarly, a lower PV integration cost indicates a better utilization of PV resources and a stronger economic viability.

Three scenarios were established to validate the proposed model through comparative testing.

Case 1: Installed distributed PV power sources without ES.

Case 2: Installed distributed PV power sources with ES.

Case 3: Installed distributed PV power sources with ES and DR strategies implemented to adjust loads.

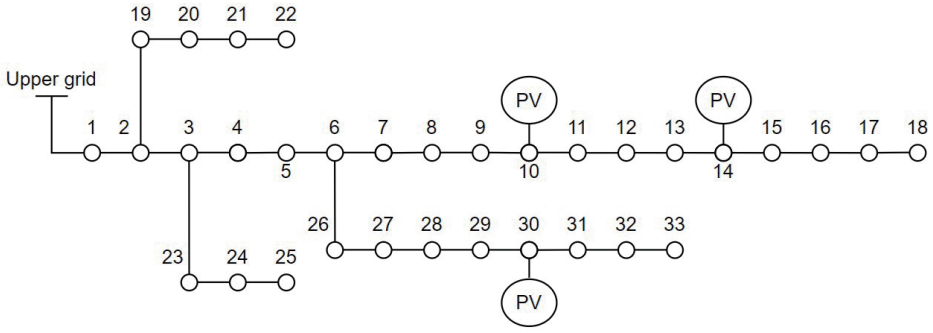

Fig. 2. Distribution network topology.

Table 2
Electricity price.

Items	Time	Price (CNY$/kWh)
Electricity	1:00–7:00, 23:00–24:00	0.1
	8:00–18:00	0.5
	19:00–22:00	0.9

Table 3
Parameters of ES and system specifications.

Parameters	Value
(a) ES	
Investment price per unit of ES capacity (CNY$/kWh)	500
Running costs per unit of exchanged electricity (CNY$/kWh)	0.1
Planned operating life (years)	20
Discount factor	0.5
(b) System	
Cost of network loss (CNY$/kWh)	0.5
Rated voltage of nodes (p.u.)	1
Branch circuit capacity limitation (kVA)	0–5000
Voltage limitation of nodes (p.u.)	0.9–1.1
DR strategy subsidy costs (CNY$/kWh)	0.08

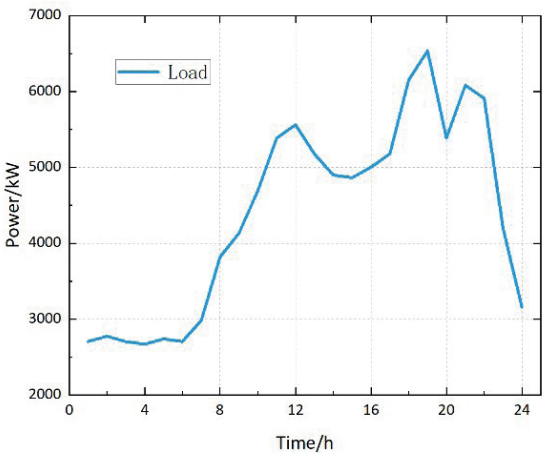

Fig. 3. (Color online) Daily load curve.

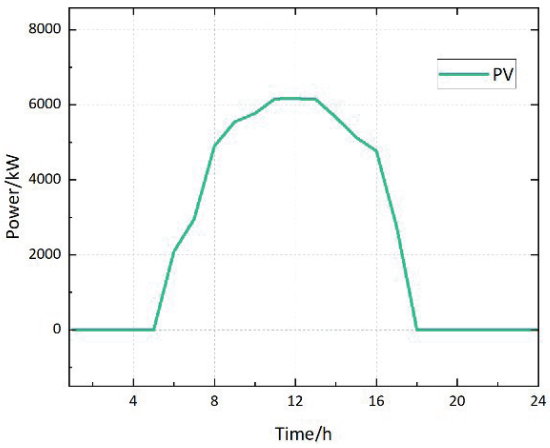

Fig. 4. (Color online) PV output curve.

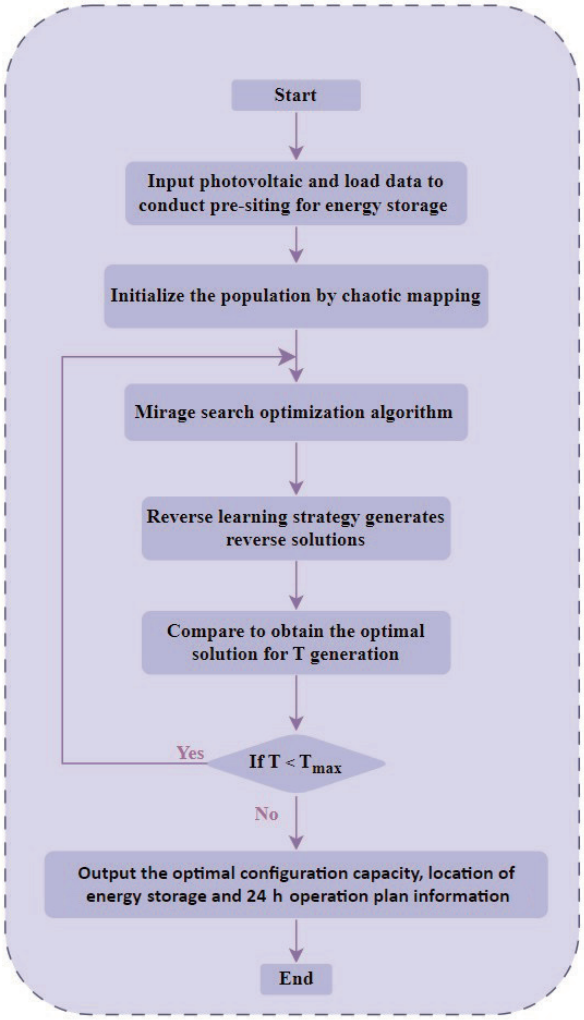

Fig. 5. (Color online) Program flowchart.

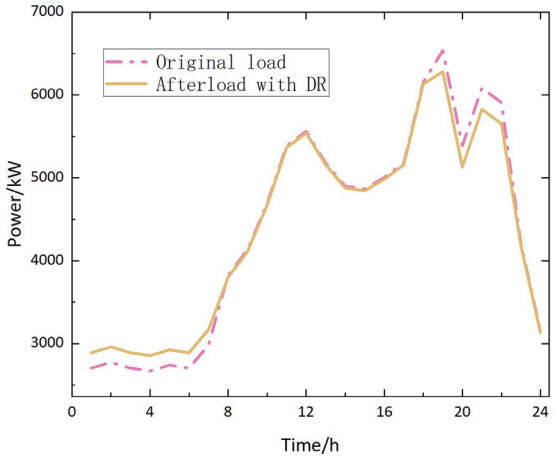

Fig. 6. (Color online) Load before and after DR.

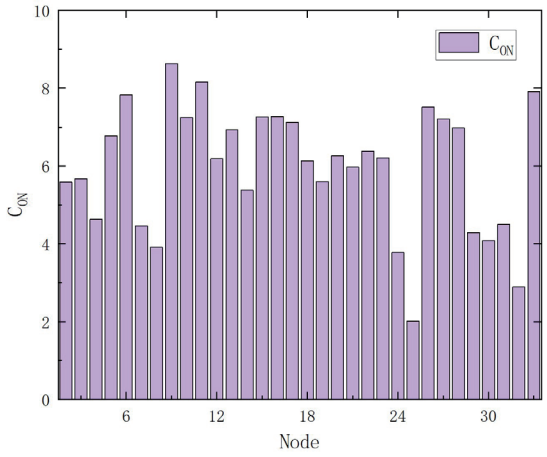

Fig. 7. (Color online) Chart for comparison of ES pre-location.

The configuration details for each case are presented in Table 4, and the specific cost compositions are shown in Table 5.

In Case 1, no ES was installed, resulting in the majority of costs coming from electricity purchased from the upper grid. Compared with Case 1, Cases 2 and 3 incorporate planned ES, which introduces additional operational and investment costs for the ES. However, these cases exhibit reductions in power purchase costs by 5.57 and 8.49%, and in PV integration cost by 6.28 and 8.78%, respectively. Case 3 further includes a DR strategy, which adds compensation cost for implementing DR. Nevertheless, it leads to further reductions in various types of costs compared with Case 2. In terms of total cost, Case 2 with the ES system shows a cost reduction of 5.31%, while Case 3, which includes the additional DR strategy, achieves a cost reduction of 8.19%. These results demonstrate that the proposed configuration model enhances both the economic efficiency of the system and the capability of PV integration.

Figure 8 presents the 24 h charging/discharging schedule of the ES system within the distribution network. Taking Case 2 as an example, from 00:00 to 05:00, when the network load is low, the ES system discharges to utilize its remaining energy. Between 06:00 and 07:00, as load increases and PV output growth is insufficient, the storage continues discharging at a low

Table 4
ES configuration.

	Location	Capacity/kW
Case 1	—	—
Case 2	33	1076.47
Case 3	33	873.22

Table 5
Results for each case.

	F1	F2	F3	F4	F5	F6	Total
Case 1	6493.91	—	—	29094.34	2754.06	—	38342.31
Case 2	6085.80	737.53	264.17	27473.73	1744.39	—	36305.62
Case 3	5923.93	598.28	222.08	26623.64	1728.25	103.84	35200.02

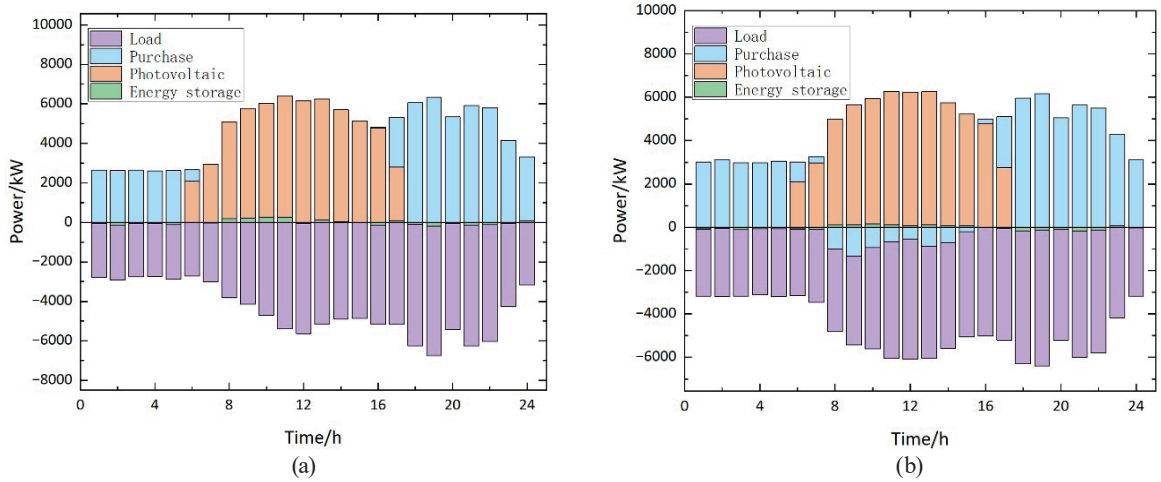

Fig. 8. (Color online) Charge–discharge schedule chart in 24 h ES Cases (a) 2 and (b) 3.

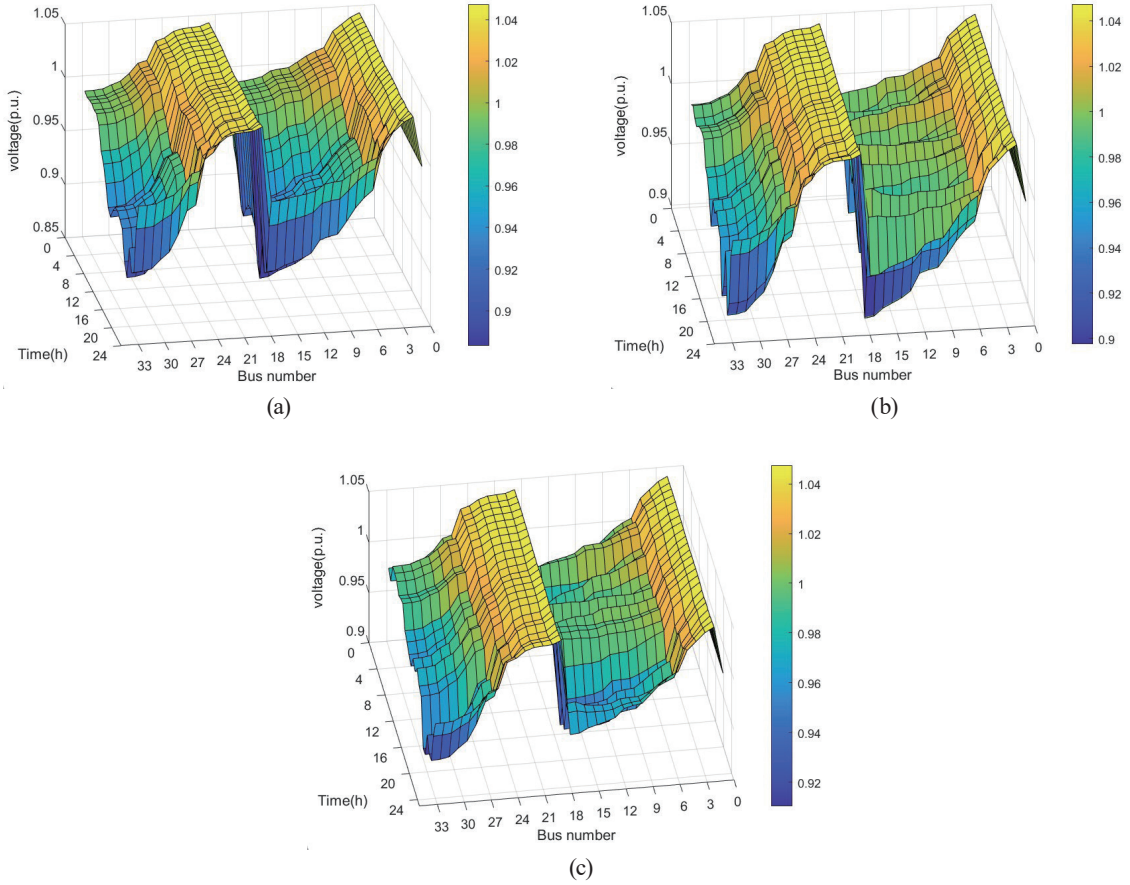

Fig. 9. (Color online) IEEE 33-bus test system within 24 h voltage distribution. Cases (a) 1, (b) 2, and (c) 3.

power level. From 08:00 to 17:00, with sufficient PV output, the storage switches to the charging mode to absorb surplus power. During the load peak from 18:00 to 22:00, it discharges again to alleviate network pressure. Finally, from 23:00 to 24:00, it discharges during the low-load period while preparing for the next cycle.

The 24 h voltage distribution at various nodes of the distribution network is shown in Fig. 9. It is evident that the voltage levels at all nodes during the 24 h period have been significantly improved after integrating ES into the operation. A satisfactory power quality is ensured because no node voltages exceed the specified limit. On comparing Fig. 9(a) with Figs. 9(b) and 9(c), it is clear that with the installation of ES, the system voltage remains largely stable at around the standard voltage level. This validates the effectiveness of ES in enhancing the voltage level of the distribution network.

5. Conclusions

An ES optimization allocation system for PV absorption capacity in distribution grids has been successfully developed in this study. By utilizing irradiance data from PV sensors and integrating load data, the model determines optimal ES configurations and 24 h charging/

discharging schedules. Therefore, an evaluation framework using PV absorption cost metrics can effectively balance the system's PV absorption capacity and economic efficiency. Here, the model computational efficiency using the MSO algorithm is improved to achieve the optimal ES configuration. In comparative analysis with several classic test functions and various traditional algorithms, the proposed model presents superior convergence speed and higher accuracy. The proposed system exhibits not only enhanced PV absorption rates but also reduced operational costs by approximately 8.19%. Future research may further incorporate diverse load types into DR. The system's comprehensive performance in balancing PV absorption capacity and economic efficiency can be validated under more complex grid scenarios.

Acknowledgments

This study was supported by Project No. 202305B029, the Tianjin Carbon Peak and Carbon Neutrality Technology Major Project (Grant no. 24ZXTKSN00030), and the Tianjin Natural Science Foundation Project (Grant no. 23JCQNJC01060).

References

1 Y. Liu, E. Duran, A. Bruce, B. Yildiz, B. Mendonca Severiano, I. Anwar Ibrahim, J. Rispler, C. Martell, and F. Rougieux: Appl. Energy **401** (2025) 126636. https://doi.org/10.1016/j.apenergy.2025.126636
2 J. Zhang, T. Wang, Z. Liao, Z. Tang, Y. Pei, Q. Cui, J. Shu, and W. Zheng: Energy **325** (2025) 136191. https://doi.org/10.1016/j.energy.2025.136191
3 S. Fan, H. Geng, and H. Zhang: Solar Energy **298** (2025) 113572. https://doi.org/10.1016/j.solener.2025.113572
4 Y. Liu, X. Liu, L. Guo, Z. Wang, H. Yu, Y. Wang, and C. Wang: J. Energy Storage **136** (2025) 118418. https://doi.org/10.1016/j.est.2025.118418
5 L. Mo, Y. He, T. Xu, and M. Zuo: J. Energy Storage **133** (2025) 117774. https://doi.org/10.1016/j.est.2025.117774
6 Z. Wang, Y. Jia, X. Han, P. Wang, and J. Liu: Appl. Energy **394** (2025) 126130. https://doi.org/10.1016/j.apenergy.2025.126130
7 R. Feng, K. Wang, X. Xu, Z.-T. Yu, and Q. Lin: Appl. Energy **364** (2024) 123164. https://doi.org/10.1016/j.apenergy.2024.123164
8 K. Kang, H. Jia, H. Hui, and D. Liu: Appl. Energy **394** (2025) 126174. https://doi.org/10.1016/j.apenergy.2025.126174
9 Y. Wang and J. Wu: Energy **311** (2024) 133376. https://doi.org/10.1016/j.energy.2024.133376
10 Y. Wu, Z. Li, X. Xiao, and S. Golshannavaz: J. Energy Storage **104** (2024) 114501. https://doi.org/10.1016/j.est.2024.114501
11 P. K. BOGGARAPU, D. S. Pillai, N. Rajasekar, C. Manickam, and S. I. Ganesan: IEEE Trans. Ind. Electron. **68** (2020) 2998750. https://doi.org/10.1109/tie.2020.2998750
12 N. Kumar, B. Singh, and B. K. Panigrahi: IEEE Trans. Transp. Electrif. **9** (2023) 2583. https://doi.org/10.1109/tte.2022.3213253
13 X. Sun, L. Lin, S. Wu, X. Zhai, C. Jin, and X. Pan: J. Energy Storage **133** (2025) 117949. https://doi.org/10.1016/j.est.2025.117949
14 N. Sheikhghaffari, A. Ebrahimi, and B. Ghorbani: Cryogenics **141** (2024) 103878. https://doi.org/10.1016/j.cryogenics.2024.103878
15 J. Wang, Y. Wen, K. Wu, S. Ding, Y. Liu, H. Tian, J. Zhang, L. Wang, Q. Cao, and Y. Zhang: J. Energy Storage **93** (2024) 112298. https://doi.org/10.1016/j.est.2024.112298
16 S. H. Nengroo, S. Lee, M. F. Shaaban, and D. Har: J. Energy Storage **95** (2024) 112489. https://doi.org/10.1016/j.est.2024.112489
17 W. Wang, C. Li, Y. He, H. Bai, K. Jia, and Z. Kong: Energy **311** (2024) 133330. https://doi.org/10.1016/j.energy.2024.133330
18 J. He, S. Zhao, J. Ding, and Y. Wang: Adv. Eng. Software **203** (2025) 103883. https://doi.org/10.1016/j.advengsoft.2025.103883